Binaries wandering around supermassive black holes due to gravitoelectromagnetism

Xian Chen[1,2,*] and Zhongfu Zhang[1]

[1]*Department of Astronomy, School of Physics, Peking University, 100871 Beijing, China*
[2]*Kavli Institute for Astronomy and Astrophysics at Peking University, 100871 Beijing, China*

(Received 20 June 2022; accepted 14 November 2022; published 30 November 2022)

Extreme-mass-ratio inspirals are important sources for space-borne gravitational-wave detectors. Such a source normally consists of a stellar-mass black hole (BH) and a Kerr supermassive BH (SMBH), but recent astrophysical models predict that the small body could also be a stellar-mass binary BH (BBH). A BBH reaching several gravitational radii of a SMBH will induce rich observable signatures in the waveform, but the current numerical tools are insufficient to simulate such a triple system while capturing the essential relativistic effects. Here we solve the problem by studying the dynamics in a frame freely falling alongside the BBH. Since the BBH is normally nonrelativistic and much smaller than the curvature radius of the Kerr background, the evolution in the free-fall frame reduces essentially to Newtonian dynamics, except for a perturbative gravitoelectromagnetic force induced by the curved background. We use this method to study the BBHs on near-circular orbits around a SMBH and track their evolution down to a distance of 2–3 gravitational radii from the SMBH. Our simulations reveal a series of dynamical effects that are not shown in the previous studies using conventional methods. The most notable one is a radial oscillation and azimuthal drift of the BBH relative to the SMBH. These results provide new insight into the evolution and detection of the extreme-mass-ratio inspirals containing BBHs.

DOI: 10.1103/PhysRevD.106.103040

I. INTRODUCTION

The idea that two stellar-mass compact objects ($\sim 10M_\odot$) could form a binary and merge near a supermassive black hole (SMBH, $\gtrsim 10^6 M_\odot$) is an old one. It could date back to the 1970s, soon after Weber reported a strong signal in his gravitational-wave (GW) experiment [1]. Several authors proposed that the signal could come from a GW source, such as a merging binary, near the innermost stable circular orbit (ISCO) around the SMBH in the Galactic Center [2–4]. The signal appeared strong because it was gravitationally lensed by the SMBH. This idea, however, went largely unnoticed since the controversy of Weber's result.

The recent observations of GWs by the Laser Interferometer Gravitational-wave Observatory (LIGO) and the Virgo detectors has revived the interest in the very same idea. So far, LIGO and Virgo have detected nearly 100 binary black holes (BBHs) [5]. The majority of them seem significantly more massive than the black holes (BHs) found previously in x-ray binaries. The sharp contrast raises an interesting question about the origin of these massive objects. More than one astrophysical channels may be responsible for producing them (see [6–8] for summaries). Among the many possibilities is a BBH orbiting around and dynamically interacting with a SMBH.

On one hand, the SMBH could accelerate the merger of the BBH by exciting its eccentricity, due to either the Von Zeipel–Lidov-Kozai mechanism when the mutual inclination of the triple system is high [9–11], or the evection resonance when the inclination is small [12–15]. In either case, the postmerger BH is likely retained in the vicinity of the SMBH due to the large escape velocity, and hence could participate in another merger [16]. The repeated mergers could explain the large BH mass detected by LIGO/Virgo. On the other, if the SMBH has an accretion disk, as would be the case in an active galactic nucleus (AGN), a BH embedded in the disk could grow by accreting the surrounding gas. More importantly, BBHs could form and merge more frequently in the assistance of the gas [17–20]. Interaction with the other compact objects in the accretion disk may further enhance the merger rate of BBHs [21,22]. It has been shown that the merger rate could be comparable to the LIGO/Virgo event rate in the above astrophysical scenarios [23–30].

The GW signal from such a BBH orbiting a SMBH is the focus of many recent studies. It has been shown that the GWs emitted from the BBH will be periodically modulated by the Doppler shift [31–34] as well as an aberrational effect [35]. This modulation may be negligible for a LIGO/Virgo event, because the signal is too short (< 1 s) compared with

*Corresponding author.
xian.chen@pku.edu.cn

the orbital period around the SMBH, therefore does not allow the velocity of the c.m. of the BBH to substantially change [36]. However, the effect is detectable by the space-borne Laser Interferometer Space Antenna (LISA), because LISA could track a BBH for as long as several years [37]. The long waveform can also reveal the variation of the internal eccentricity of the BBH, which is induced by the aforementioned Von Zeipel–Lidov-Kozai cycle [32,38–41]. If the SMBH is spinning, then the frame-dragging effect will further perturb the BBH and leave a detectable imprint in the GW signal [42,43].

These earlier studies normally assume that the BBH is hundreds to thousands of gravitational radii away from the SMBH. This assumption is partly motivated by the earlier theoretical predictions (e.g., [9,18]) and partly due to a practical reason, that is the relativistic effect at such intermediate distances is mild so that it can be modeled with the post-Newtonian (PN) formalism [44]. However, more recent studies suggest that the BBH could reach a distance as small as ten gravitational radii from the SMBH, due to the interaction with other stars in the nuclear star cluster or an accretion disk surrounding the SMBH [29,45–47]. Such events are expected to come mainly from extra galaxies, and the event rate is estimated to be between 0.03 and 0.4 $\mathrm{Gpc}^{-3}\,\mathrm{yr}^{-1}$ depending on the formation channel [45,47]. The fact that the upper limit could account for $(1-2)\%$ of the current LIGO/Virgo detection rate [48] indicates that one or two BBHs out of the ∼100 detected events may come from the vicinities of SMBHs. Such a system resembles in many ways an important category of LISA sources, known as extreme-mass-ratio inspirals (EMRIs) [49]. But the distinction is also clear. Instead of having only one stellar-mass BH, now the system contains two stellar-mass BHs, bound by their self-gravity.

As the distance between the BBH and the SMBH decreases, interesting phenomena emerge, which have attracted intense scrutiny lately. (i) The Doppler and gravitational redshift becomes so strong that in the detector frame the BBH will appear more massive and more distant [50]. The same effect can also lower the observed GW frequency of a binary neutron star and make its detection easier for ground-based observatories [51]. (ii) The large spacetime curvature around the SMBH could bend the null geodesics of the GWs emitted by the BBH, producing lensed images [52,53], echoes [54], as well as a Shapiro delay [55]. If the SMBH is spinning and the BBH lies in the equatorial plane, then the GWs leaving the BBH may be amplified by a Penrose-like process [56]. (iii) When the frequency of the GWs from the BBH matches a quasinormal mode of the SMBH, the SMBH could be resonantly excited [57]. (iv) The fast motion of the BBH around the SMBH can distort the pattern of its GW radiation due to aberration, which will induce additional higher modes in the GW signal [58]. (v) Since the coalescence of the BBH produces high-frequency GWs $(10-10^2$ Hz) and its motion around the SMBH generates low-frequency ones ($\sim 10^{-3}$ Hz), the triple system at its final evolutionary stage becomes a multiband GW source. Such a source is ideal for measuring the energy and momentum carried away by GWs, as well as constraining the mass of gravitons [59].

Despite the increasing interest in considering a smaller separation between the BBH and the SMBH, the numerical tools we have today may not be adequate to model the dynamics of such a triple system. The commonly used PN approximation breaks down as the separation shrinks to the order of ten gravitational radii because the velocity of the BBH relative to the SMBH becomes a significant fraction of the speed of light. A more subtle issue is that many earlier studies, in order to simplify the computation of the waveform, treated the BBH as a single body and modeled its orbit around the SMBH with a geodesic line (e.g., [40,41]). The validity of this treatment has not been tested when the separation is so small. In the end, a binary has internal structures and for this reason differs from a test particle.

One possible solution is to take advantage of the equivalence principle and investigate the problem in a frame freely falling together with the BBH. Especially when the BBH is nonrelativistic, the dynamics in this free-fall frame (FFF) is essentially Keplerian, except for a perturbing force induced by the curvature of the SMBH background. We notice that a similar method has been used to model a binary star close to a Schwarzschild SMBH [60], though in their work the authors implicitly assumed that the c.m. of the binary follows a geodesic line. Here we revise their method to simulate the evolution of a BBH down to a distance of 2–3 gravitational radii from a Kerr SMBH and, at the same time, self-consistently track the c.m. of the BBH, which turns out to be nongeodesic.

The paper is organized as follows. In Sec. II we describe the theoretical framework of simulating the evolution of the BBH in its FFF. Based on the observation that the perturbation by the Kerr background induces gravitoelectromagnetic (GEM) forces in the FFF, we argue that these GEM forces will drive the c.m. of the BBH away from a geodesic line. In Sec. III we carry out numerical simulations to test our prediction. We also analyze the evolution in different frames to better understand the cause and the effects of the geodesic deviation. In Sec. IV we vary the initial conditions to showcase the richness of the dynamical effects induced by the close interaction between the BBH and the SMBH. In Sec. V, we also compare our results with those derived from PN and Newtonian simulations to highlight the difference. Based on our simulation results, we discuss in Sec. VI the possible observational signatures imprinted in the GW signal of such a triple system. Finally, we conclude in Sec. VII and point out several caveats of the current work, as well as their possible solutions. Throughout the paper, we use geometrized units where $G = c = 1$.

II. THEORY

A. Equation of motion

The system of our interest consists of a SMBH with a mass of M ($10^6 \lesssim M \lesssim 10^9$) and a BBH within a distance of $r \lesssim 10M$ from the SMBH. Following the convention, we refer to the self-gravitating BBH as the "inner binary" and the trajectory of its c.m. around the SMBH as the "outer orbit." We consider a rotation of the SMBH and denote the dimensionless spin parameter as s. We further denote the masses of the two BHs of the BBH as m_1 and m_2. Then the total mass of the inner binary is $m_{12} = m_1 + m_2$, which is typically tens of solar masses.

Although the outer orbit is highly relativistic, the inner one is much simpler. On one hand, the semimajor axis of the inner binary, which we denote by a, is 10^2–10^3 times smaller than r [45–47], and hence also much smaller than the curvature radius of the background Kerr metric. This fact indicates that the spacetime is sufficiently flat sufficiently close to the BBH. On the other hand, a is typically 10^3–10^4 times greater than m_{12}, so that the relative speed between the two small BHs ($\sim\sqrt{m_{12}/a}$) is nonrelativistic.

Given the above hierarchy, it is the most convenient to use the Fermi normal coordinates to describe the inner orbit [60]. They are the coordinates a free-fall observer would naturally choose since sufficiently close to the observer the metric is approximately Minkowskian. We denote these coordinates as $(\tau, \mathbf{x}) = (\tau, x, y, z)$, where the origin of the spatial coordinates coincides with the location of the observer.[1] In such a frame, the perturbation to the Minkowski metric by the SMBH is of the order of $(\mathbf{x}/r)^2$, which is small in our case of $|\mathbf{x}| \simeq a \ll r$. We choose the origin of the FFF (the free-fall observer) to coincide with and has the same velocity as the c.m. of the BBH. Then the initial velocities of the BHs in the FFF are Keplerian, and our problem reduces essentially to Newtonian dynamics. We note that the origin of the FFF by construction follows a geodesic line, but the c.m. of the BBH does not necessarily follow the same geodesic, as we will show later.

The aforementioned quadratic-order perturbation to the Minkowskian metric induces GEM forces in the FFF [61]. These forces can be formulated with

$$\mathbf{F} = -m\mathbf{E} - 2m\mathbf{v} \times \mathbf{B}, \tag{1}$$

where m is the rest mass of an object, $\mathbf{v} \coloneqq d\mathbf{x}/d\tau$ is its velocity in the FFF, and $\mathbf{E}$ and $\mathbf{B}$ are, respectively, the gravitoelectric and gravitomagnetic fields. The minus signs in the above equation reflect the fact that mass has a negative charge in gravitoelectromagnetism. To first order in $\mathbf{x}$, the components of the GEM fields can be calculated with

$$E_i(\tau, \mathbf{x}) = R_{0i0j}(\tau)x^j, \tag{2}$$

$$B_i(\tau, \mathbf{x}) = -\frac{1}{2}\epsilon_{ijk}R^{jk}{}_{0l}(\tau)x^l, \tag{3}$$

where R_{0i0j} and $R^{jk}{}_{0l}$ are the components of the Riemann tensor, ϵ_{ijk} is the Levi-Civita symbol, and i, j, k, and l are spatial indices which take the values 1,2,3.

Combining the Newtonian and GEM forces, we can write the equation of motion in the FFF as

$$m_a\frac{d^2\mathbf{x}_a}{d\tau^2} = -m_a m_b\frac{\mathbf{x}_a - \mathbf{x}_b}{|\mathbf{x}_a - \mathbf{x}_b|^3} + \mathbf{F}_a(\tau, \mathbf{x}_a, \mathbf{v}_a), \tag{4}$$

where a, $b = 1, 2$, denoting the two stellar-mass BHs. We note that the last equation is valid even when the c.m. of the BBH deviates from the origin of the FFF. The validity of this equation only requires that the position of the c.m., $\mathbf{x}_{\text{c.m.}} = (m_1\mathbf{x}_1 + m_2\mathbf{x}_2)/m_{12}$, satisfies the condition $|\mathbf{x}_{\text{c.m.}}| \ll r$. Otherwise, if the BBH wanders too far away from the origin of the FFF, the perturbation term $(\mathbf{x}/r)^2$ in the metric will no longer be small and the formulas for the GEM fields will be invalid.

B. Calculating the gravitoelectromagnetic forces

Although it is the simplest to write the equation of motion in the FFF, it is not straightforward to calculate the GEM fields in the same frame. This is caused by the fact that the Riemann tensor is conventionally derived in the "locally nonrotating frame" (LNRF [62]), a frame not in free fall. Here we will show that the FFF in general differs from the LNRF by a boost and a rotation. Based on this understanding, we will derive the GEM forces in the FFF.

We start from the well-known Boyer-Lindquist coordinates (t, r, θ, ϕ) in which the metric is

$$\begin{aligned} ds^2 = &-(1-2Mr/\Sigma)dt^2 - (4Msr\sin^2\theta/\Sigma)dtd\phi + (\Sigma/\Delta)dr^2 \\ &+ \Sigma d\theta^2 + (r^2 + s^2 + 2Ms^2r\sin^2\theta/\Sigma)\sin^2\theta d\phi^2, \end{aligned} \tag{5}$$

and the functions Δ, Σ, and A are defined by

$$\begin{aligned} \Delta &\coloneqq r^2 - 2Mr + s^2, \\ \Sigma &\coloneqq r^2 + s^2\cos^2\theta, \\ A &\coloneqq (r^2 + s^2)^2 - s^2\Delta\sin^2\theta. \end{aligned} \tag{6}$$

The bases of the Boyer-Lindquist coordinates are not orthonormal. Therefore, it is not easy to derive the Riemann tensor in this frame.

On the contrary, the LNRF has orthonormal coordinates. It is the frame used by an observer whose world line follows constant r and θ but different ϕ, when viewed from the Boyer-Lindquist coordinates. The coordinates of the

[1] Here we use τ to label the time in the free-fall frame, and we save the symbol t to denote the time in the Boyer-Lindquist coordinate.

LNRF, $(X^t, X^r, X^\theta, X^\phi)$, is related to the Boyer-Lindquist coordinates as

$$\begin{aligned} dX^t &= (\Sigma\Delta/A)^{1/2}dt, \\ dX^r &= (\Sigma/\Delta)^{1/2}dr, \\ dX^\theta &= \Sigma^{1/2}d\theta, \\ dX^\phi &= -\frac{2Msr\sin\theta}{(\Sigma A)^{1/2}}dt + \left(\frac{A}{\Sigma}\right)^{1/2}\sin\theta d\phi. \end{aligned} \tag{7}$$

It has been shown that the Riemann tensor is much simpler to derive in the LNRF than in the Boyer-Lindquist coordinates [62]. In the following, we denote the Riemann tensor in the LNRF as $R_{\mu\nu\rho\sigma}$.

To transform $R_{\mu\nu\rho\sigma}$ into the FFF, we notice that at any instance in time, the local frame of a free-fall observer differs from the LNRF at the observer's location by a Lorentz transformation [62]. Therefore, given the velocity of the FFF relative to the LNRF, we can in principle derive the Riemann tensor in the FFF by a Lorentz transformation. However, because the velocity in general is not aligned with any of the spatial axes of the LNRF, the Lorentz transformation will be a complicated one.

In practice, we can simplify the Lorentz transformation according to the problem we are dealing with. We notice that BBHs could be delivered to the vicinities of spinning SMBHs along near-circular orbits in the equatorial planes of the SMBHs. This situation has been predicted by the previous models related to AGNs, and the corresponding event rate is estimated to be about 0.4 $\mathrm{Gpc^{-3}\,yr^{-1}}$ [47]. In this case, it is natural to choose a free-fall observer on a circular orbit in the equatorial plane. Viewed from the LNRF, this observer is moving in the azimuthal (X^ϕ) direction. The speed is

$$u = \frac{\pm M^{1/2}(r \mp 2sM^{1/2}r^{1/2} + s^2)}{\Delta^{1/2}(r^{3/2} \pm sM^{1/2})}, \tag{8}$$

where the upper signs refer to prograde orbits and the lower ones refer to retrograde orbits [62]. Given these conditions, the simplest coordinate system the free-fall observer can use to calculate the Riemann tensor is such that one spatial axis is in the same direction as the velocity (X^ϕ direction), and the other two are aligned, respectively, with the X^r and X^θ axes of the LNRF. Then the Lorentz transformation matrix has the simple form

$$\Lambda^{\mu}_{\mu'} = \begin{pmatrix} \gamma & 0 & 0 & \gamma\beta \\ 0 & 1 & 0 & 0 \\ 0 & 0 & 1 & 0 \\ \gamma\beta & 0 & 0 & \gamma \end{pmatrix}, \tag{9}$$

where $\beta = u/c$, $\gamma = \sqrt{1-\beta^2}$ is the Lorentz factor, and the primed index μ' refers to a coordinate in the boosted (observer's) frame. The transformation of the Riemann tensor, $R_{\mu'\nu'\rho'\sigma'} = \Lambda^{\mu}_{\mu'}\Lambda^{\nu}_{\nu'}\Lambda^{\rho}_{\rho'}\Lambda^{\sigma}_{\sigma'}R_{\mu\nu\rho\sigma}$, is also significantly simplified.

However, to appropriately use the Riemann tensor $R_{\mu'\nu'\rho'\sigma'}$, we must notice a subtle but important difference between the frame where $R_{\mu'\nu'\rho'\sigma'}$ is derived and the FFF where the equation of motion, i.e., Eq. (4), applies. The FFF uses Fermi normal coordinates that, by construction, form an inertial frame along the entire geodesic of the free-fall observer. However, $R_{\mu'\nu'\rho'\sigma'}$ and the corresponding GEM fields are calculated in a different frame, which is a Lorentz boost of the LNRF in a specific direction. Such a boosted frame is an inertia frame only locally, at one instance in time, but not along the entire geodesic because the direction of the boost changes with time. For example, consider a free gyro placed at the origin of this boosted frame. As the gyro moves along a geodesic around the SMBH, its spin axis is fixed in the FFF but in general will precess relative to the spatial coordinates of the LNRF, as well as the boosted frame. For this reason, the boosted frame is also known as the "local inertial frame" (LIF).

The relationship between the LNRF, LIF, and FFF is illustrated in Fig. 1, where we have considered a circular orbit for the free-fall observer. The rotation of the LIF relative to the FFF is clearly shown. The corresponding angular velocity viewed from the FFF can measured by the precession of a free gyro, and is $\omega = -\sqrt{M/r^3}$ [63]. The minus sign indicates that the angular velocity vector $\boldsymbol{\omega}$ is pointing in the $-y$ direction when the free-fall observer is moving on a prograde orbit around the Kerr SMBH.

Having understood the relationship between the LIF and FFF, we can derive the GEM forces in the FFF as follows.

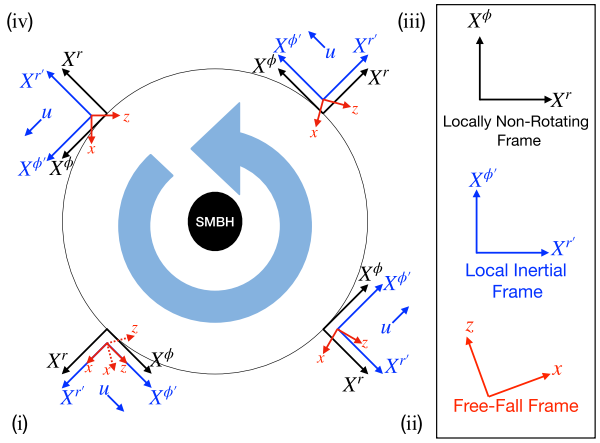

FIG. 1. Different reference frames used in this paper and their relative orientation as they rotate around the SMBH. The curved cyan arrow shows the direction of rotation and the Roman numerals indicate the sequence of the evolution. The red dotted arrows mark the x and z axes of the free-fall frame when it has completed one revolution around the SMBH. The axes misalign with the original ones because of precession.

Given the mass m, position $\mathbf{x} = (x, y, z)$, and velocity $\mathbf{v}$ of an object in the FFF, we first calculate its position $\mathbf{x}' = (X^{r'}, X^{\theta'}, X^{\phi'})$ and velocity $\mathbf{v}'$ in the LIF with

$$X^{r'} = x\cos(\omega\tau) - z\sin(\omega\tau), \tag{10}$$

$$X^{\theta'} = y, \tag{11}$$

$$X^{\phi'} = x\sin(\omega\tau) + z\cos(\omega\tau), \tag{12}$$

and $\mathbf{v}' = \mathbf{v} - \boldsymbol{\omega}\times\mathbf{x}$. Notice that $\omega < 0$ ($\omega > 0$) if the FFF is moving along a prograde (retrograde) circular orbit around the SMBH. The above transformation reflects the fact that the LIF differs from the FFF by a rotation. Using $\mathbf{x}'$ and the Riemann tensor $R_{\mu'\nu'\rho'\sigma'}$, we can construct the GEM fields in the LIF, namely, $\mathbf{E}'$ and $\mathbf{B}'$. Then the GEM force in the LIF, $\mathbf{F}' = (F_{r'}, F_{\theta'}, F_{\phi'})$, is computed with $\mathbf{F}' = -m\mathbf{E}' - 2m\mathbf{v}'\times\mathbf{B}'$. Finally, rotating $\mathbf{F}'$ around the $X^{\theta'}$ axis by an angle of $\omega\tau$, we get the GEM force in the FFF. Mathematically, the rotation is performed with

$$F_x = F_{r'}\cos(\omega\tau) + F_{\phi'}\sin(\omega\tau), \tag{13}$$

$$F_y = F_{\theta'}, \tag{14}$$

$$F_z = -F_{r'}\sin(\omega\tau) + F_{\phi'}\cos(\omega\tau). \tag{15}$$

C. Deviation from free fall

We notice that one assumption which is implicitly adopted by many earlier works is that the outer orbit follows the geodesic of a test particle (e.g., [40–43]). If this assumption is valid, then we can find a FFF whose origin always coincides with the c.m. of the BBH. We will show in this subsection that it is not the case because of the existence of the gravitomagnetic force.

In the FFF defined above, the total force exerted on the c.m. of the BBH is $m_1 d^2\mathbf{x}_1/d\tau^2 + m_2 d^2\mathbf{x}_2/d\tau^2$. Now consulting Eq. (4), we can immediately eliminate the total force due to Newtonian gravity because the gravitational forces on the two stellar-mass BHs are of the same magnitude but in opposite directions. As for the GEM force, i.e., the second term on the right-hand side of Eq. (4), we first notice that the gravitoelectric field, $\mathbf{E}_a$, is proportional to the position $\mathbf{x}_a$ of an object. Therefore, the total gravitoelectric force, $\mathbf{F}^E_{\rm c.m.} = -m_1\mathbf{E}_1 - m_2\mathbf{E}_2$, scales with $m_1\mathbf{x}_1 + m_2\mathbf{x}_2$, which is $m_{12}\mathbf{x}_{\rm c.m.}$. As a result, if at one instance we choose the origin of the FFF to coincide with the c.m. of the BBH, then the total gravitoelectric force will vanish. In summary, the self-gravity and the gravitoelectric force will not induce acceleration to the c.m. if initially we place the BBH at $\mathbf{x}_{\rm c.m.} = 0$ in the FFF. Consequently, these forces will not cause the outer orbit to deviate from the geodesic of a test particle.

The effect of gravitomagnetic force is different because the force, $-2m\mathbf{v}\times\mathbf{B}$, is not a linear function of the position $\mathbf{x}$. For example, consider an initial condition of $\mathbf{x}_{\rm c.m.} = 0$. This condition leads to $m_1\mathbf{B}_1 + m_2\mathbf{B}_2 = 0$ because $\mathbf{B}_a$ is a linear function of $\mathbf{x}_a$. From the above relationship, we further derive

$$\mathbf{F}^B_{\rm c.m.} = \sum_{a=1}^{2} -2m_a(\mathbf{v}_a - \boldsymbol{\omega}\times\mathbf{x}_a)\times\mathbf{B}_a, \tag{16}$$

$$= 2m_2\boldsymbol{\omega}\times(\mathbf{x}_2 - \mathbf{x}_1)\times\mathbf{B}_2 - 2m_2(\mathbf{v}_2 - \mathbf{v}_1)\times\mathbf{B}_2, \tag{17}$$

where $\mathbf{B}_2$ denotes the gravitomagnetic field at the position of $\mathbf{x}_2$. The last equation shows that the total gravitomagnetic force $\mathbf{F}^B_{\rm c.m.}$ depends not on $\mathbf{x}_{\rm c.m.}$, but on the relative position $\mathbf{x}_2 - \mathbf{x}_1$ and the relative velocity $\mathbf{v}_2 - \mathbf{v}_1$ of the two small BHs. Neither of them is zero. Therefore, $\mathbf{F}^B_{\rm c.m.}$ in general does not vanish.

Now we can understand why the c.m. of the BBH does not follow a geodesic. This is because the nonvanishing gravitomagnetic force will inevitably drive the c.m. of the BBH away from the origin of the FFF, even if initially $\mathbf{x}_{\rm c.m.} = 0$. Furthermore, a small displacement in $\mathbf{x}_{\rm c.m.}$ will be quickly amplified by the gravitoelectric force because the magnitude of the force scales with $m_{12}|\mathbf{x}_{\rm c.m.}|$. As the BBH revolves around the SMBH, the direction of the gravitoelectric force will, most of the time, point away from the origin of the FFF, causing the c.m. to displace further away from the geodesic of a test particle.

III. NUMERICAL SIMULATION

A. Initial conditions

Now we use numerical simulations to showcase the effects of the GEM forces on the evolution of a BBH around a SMBH. In our fiducial model, the parameters of the BHs are $M = 4\times10^6 M_\odot$, $s = 0.9$, $m_1 = 15M_\odot$, and $m_2 = 10M_\odot$. We choose such an value for M to mimic the SMBH in the Galactic Center, but the result is applicable to other SMBHs. In particular, it is worth mentioning that such a triple system is unlikely to be found in the Galactic Center because of the low event rate [45,47], but more likely to be found in extra galaxies.

Regarding the initial semimajor axes of the inner and outer orbits, we are interested in the case when (i) the GEM forces are not negligible relative to the self-gravity of the inner binary and (ii) the inner binary can withstand the tidal force of the SMBH (i.e., the gravitoelectric force). To identify the relevant values of the semimajor axes, we start from the acceleration of a test particle around a spinning SMBH,

$$\frac{d^2\mathbf{X}}{dt^2} = \mathbf{g} + \mathbf{V}\times\mathbf{H}, \tag{18}$$

which is derived in the limit of weak field and slow motion [64,65]. Here $\mathbf{V} = d\mathbf{X}/dt$ is the velocity of the particle relative to the SMBH,

$$\mathbf{H} = 2\left[\frac{\mathbf{S} - 3(\mathbf{S}\cdot\mathbf{n})\mathbf{n}}{r^3}\right] \tag{19}$$

stands for the gravitomagnetic field, $\mathbf{S}$ is the spin angular momentum of the SMBH, and $\mathbf{n}$ is the unit radial vector. Although Eq. (18) is an approximation (1.5PN), it allows us to quickly estimate the relative acceleration between m_1 and m_2 induced by the GEM forces, which is

$$\mathbf{A_{12}} = \mathbf{A}_{\rm tidal} + \delta\mathbf{V}\times\mathbf{H}_0 + \mathbf{V}_0\times\delta\mathbf{H}(r), \tag{20}$$

where the subscript 0 denotes the position of the c.m. of the inner binary. The three terms on the right-hand side of the equation are, respectively, the tidal force (i.e., the gravitoelectric force), the gravitomagnetic force caused by different velocities, and the gravitomagnetic force due to a small radial displacement. The magnitude of each term is

$$A_{\rm tidal} = \frac{2Ma}{r^3}, \tag{21a}$$

$$|\delta\mathbf{V}\times\mathbf{H}_0| = \sqrt{\frac{m}{a}}\frac{2sM^2}{r^3}, \tag{21b}$$

$$|\mathbf{V}_0\times\delta\mathbf{H}(r)| = \sqrt{\frac{M}{r}}\frac{2sM^2}{r^3}\frac{3a}{r}, \tag{21c}$$

where we have considered a coplanar triple system and assumed that $a \ll r$.

Comparing the self-gravity of the inner binary, $A_{\rm sg} \simeq m_{12}/a^2$, with the accelerations given by the last three equations, we can identify the region in the parameters space of r and a where the conditions (i) and (ii) are both satisfied. Figure 2 shows the result for our fiducial model. We find that at $r \lesssim 10M$ the two areas corresponding to the above conditions (i) and (ii) start to overlap.

In the light of Fig. 2, we set the initial semimajor axis of the BBH (inner binary) to $a_0 = 2,500m_{12}$, so that it is tidally stable as long as the binary is outside the ISCO of the SMBH. The inner orbital period is $\tau_0 = 2\pi\sqrt{a_0^3/m_{12}} \simeq$ 98 s in its rest frame. Since a_0 is much smaller than the curvature radius of the background SMBH ($\sim r$), the precision in the calculation of the GEM forces can be guaranteed. For simplicity, we assume that the inner orbit is initially circular. The corresponding GW radiation timescale is $5a_0^4/(64m_1m_2m_{12}) \simeq 50$ yrs [66], which is much longer than the mission duration of LISA. The orbital plane is chosen to be coplanar with the outer orbit, which is motivated by the prediction that BBHs could be delivered to the vicinities of SMBHs by the accretion disks of AGNs [47].

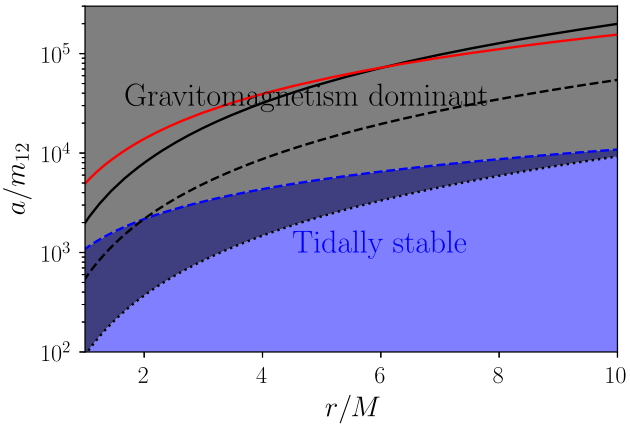

FIG. 2. The parameter space in which the inner binary (BBH) is tidally stable (blue shaded area) or the gravitomagnetic force is not negligible (gray shaded area). The blue dashed and red solid lines are derived, respectively, according to $A_{\rm sg} = 10A_{\rm tidal}$ and $A_{\rm sg} = |\mathbf{V}_0\times\delta\mathbf{H}(r)|$. The black lines are calculated according to $A_{\rm sg} = \eta|\delta\mathbf{V}\times\mathbf{H}_0|$, and the solid, dashed, and dotted ones correspond to $\eta = 1$, 10, and 100 to explore the relevant parameter space of long-term interaction. The other parameters are $M = 4\times10^6M_\odot$, $m_{12} = 25M_\odot$, and $s = 0.9$.

For the outer orbit, we adopt the initial conditions of a test particle on a circular, prograde orbit in the equatorial plane of the SMBH. Therefore, both the inner and outer orbits are inside the equatorial plane. The orbital semimajor axis is either $r = 3.3M$ or $2.8M$, to cover the region of our interest while keeping the inner binary outside the ISCO and tidally stable. The corresponding orbital periods, measured by a distant observer, are $2\pi/\Omega \simeq 866$ s and 702 s, where Ω is the orbital angular velocity in the Boyer-Lindquist coordinates [62].

B. Dynamics in the FFF

The FFF, in which we will integrate Eq. (4), is set up according to the following two requirements. (i) The origin of the FFF initially has the same position and velocity as the c.m. of the BBH. (ii) The x, y, and z axes initially align with the $X^{r'}$, $X^{\theta'}$, and $X^{\phi'}$ axes of the LIF (see Fig. 1). Such a setup allows us to use the method described in Sec. II B to simplify the calculation of the GEM forces. We note that the initial conditions we chose restrict the motion of the inner binary to the x-z plane, although the method is more general and can be used in misaligned cases.

In our fiducial model, the outer orbit initially has a radius of $r = 3.3M$. The angular momentum of the inner binary points in the $-y$ direction, so that the inner orbit rotates in the same sense as the rotation of the outer orbit. Following the previous works [67–71], we refer to this orientation as the "prograde" one. Viewed from the FFF, the inner binary initially rotates much faster than the LIF. In fact, the

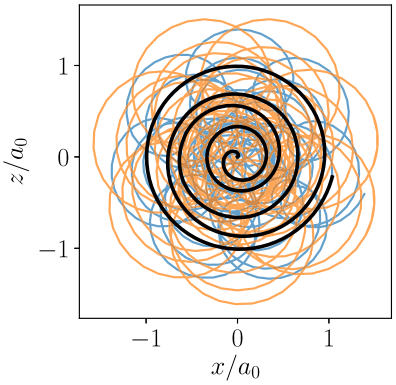

FIG. 3. Evolution of a prograde BBH in the FFF. The initial distance to the central SMBH is $r = 3.3M$. The blue and the orange curves show the trajectories of the two BHs, and the black spiral curve corresponds to the center of mass of the BBH.

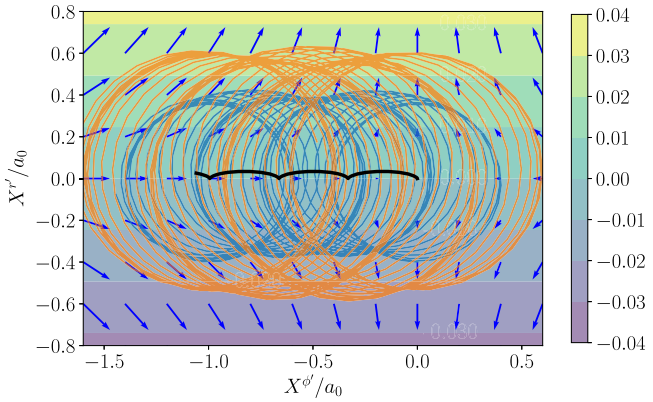

FIG. 4. Evolution of the prograde BBH in the LIF. The blue, orange, and black curves have the same meanings as in Fig. 3. The blue arrows show the direction of the gravitoelectric force acting on an object with unit mass. The length is proportional to the strength of the force. The background color indicates the strength of the gravitomagnetic field, which is perpendicular to the $X^{r'} - X^{\phi'}$ plane according to the initial conditions of our model.

angular velocity of the inner binary, $|\omega_b| = |\mathbf{v}_2 - \mathbf{v}_1|/|\mathbf{x}_2 - \mathbf{x}_1|$, is about six times greater than that of the LIF, $|\omega|$. Note that both ω_b and ω have negative values in our fiducial model. Therefore, the second term in Eq. (17) predominates, and the c.m. of the BBH will receive a gravitomagnetic force.

Figure 3 shows the evolution of the BBH in the FFF. The trajectory of the c.m. is shown as the black solid curve. Initially, the c.m. is at the origin, $(x, z) = (0, 0)$. Then it is displaced by a small amount in the positive-x direction due to the nonvanishing gravitomagnetic force. Afterwards, it spirals further away from the origin, which is driven mainly by the gravitoelectric force. The spiral pattern reflects the fact that the $\mathbf{E}$ field is rotating in the FFF with a constant angular velocity of ω due to the rotation of the LIF. This result confirms the prediction we made at the end of Sec. II C that the outer orbit does not follow a geodesic.

C. Dynamics in the LIF

To see more clearly the directions of the GEM forces, we shown in Fig. 4 the evolution of the BBH in the LIF, where the GEM fields do not rotate. In this frame, besides the self-gravity of the binary, there are four types of additional forces acting on the BHs.

(i) The gravitoelectric force is shown as the blue arrows. It vanishes only at the origin and increases with the distance from the origin.

(ii) The gravitomagnetic force is induced by the gravitomagnetic field. The $\mathbf{B}$ field is parallel to the $X^{\theta'}$ axis (pointing out of the page) and its magnitude is indicated by the color. We can see that it is linearly proportional to $X^{r'}$, which is a direct result of the simplicity of the Riemann tensor in the LIF.

To see the direction of the gravitomagnetic force, we notice that our BBH rotates clockwise in Fig. 4. Moreover, the binary remains relatively circular in our fiducial model, as is suggested by the upper panel of Fig. 5. Furthermore, the sign of the $\mathbf{B}$ field changes when one moves from the upper half-plane in Fig. 4 into the lower one. Combining the above factors, we find that the gravitomagnetic force on either BH, $-2m_a\mathbf{v}'_a \times \mathbf{B}_a$, always has a component pointing in the positive-$X^{r'}$ direction, unless $X^{r'} = 0$ in which case the $\mathbf{B}$ field vanishes. Meanwhile, the $X^{\phi'}$ component of the gravitomagnetic force oscillates between positive and negative values due to the rotation of the binary. The oscillatory component averages out to zero over one orbital period, but the

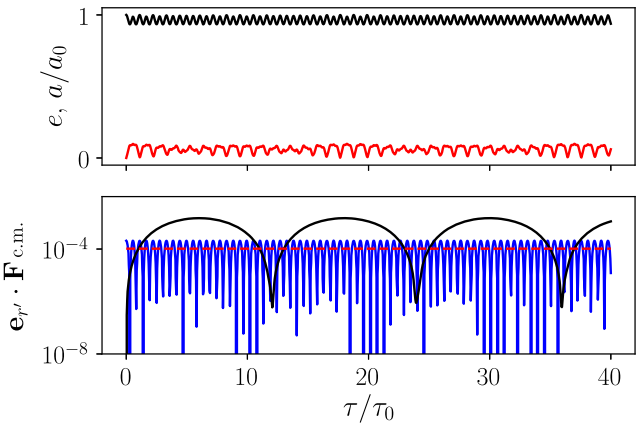

FIG. 5. Upper: evolution of the semimajor axis (black line) and eccentricity (red line) of the prograde BBH, viewed from the free-fall frame. Notice that time is in the unit of the initial orbital period τ_0 of the BBH. Lower: evolution of the radial components of the total gravitomagnetic (blue curve) and gravitoelectric (black curve) forces acting on the center of mass of the BBH. The red dashed line is the time-averaged value of the above gravitomagnetic force, computed according to Eq. (23). The values shown here are in simulation units.

$X^{r'}$ component does not. As a result, the total gravitomagnetic force acting on the c.m. of the BBH also has a nonvanishing $X^{r'}$ component.

(iii) A centrifugal force is also present because the LIF rotates with respect to the FFF, the latter of which is an inertial frame globally. The magnitude of the centrifugal force, $m\omega^2\sqrt{(X^{r'})^2+(X^{\phi'})^2}$, is also proportional to the distance to the origin, but compared with the gravitoelectric force, which is of the order of $(m\gamma^2/r^2)\sqrt{(X^{r'})^2+(X^{\phi'})^2}$, the centrifugal force is smaller by a factor of $\gamma^2(r/M)$, about 4.7 in our fiducial model.

(iv) The rotation of the LIF also induces a Coriolis force, $-m\boldsymbol{\omega}\times\mathbf{v}'$. It causes the velocity vector of a moving object to rotate counterclockwise in Fig. 4.

The black solid curve in Fig. 4 shows the trajectory of the c.m. of the BBH, which starts at the origin of the coordinates. To understand its behavior, we first notice that the gravitoelectric, centrifugal, and Coriolis forces initially do not induce any acceleration on the c.m. of the BBH, because their values depend on either $m_1\mathbf{x}_1+m_2\mathbf{x}_2$ or $m_1\mathbf{v}_1+m_2\mathbf{v}_2$, both vanish according to our initial conditions.

The only nonvanishing force acting on the c.m. is the gravitomagnetic force. We have mentioned above that it has a nonzero component pointing in the positive-$X^{r'}$ direction. To be more quantitative, we can calculate the $X^{r'}$ component of $\mathbf{F}^B_{\rm c.m.}$ according to Eq. (17). Assuming that $|\mathbf{x}_{\rm c.m.}|/a\simeq 0$ and initially the BBH is aligned with the $X^{r'}$ axis, we find that

$$\mathbf{e}_{r'}\cdot\mathbf{F}^B_{\rm c.m.}=2\mu(\omega-\omega_b)a^2R_{t'r'r'\phi'}\cos^2[(\omega_b-\omega)\tau], \quad (22)$$

where $\mathbf{e}_{r'}$ is the basis vector associated with the $X^{r'}$ axis, $\mu=m_1m_2/m_{12}$ is the reduced mass of the binary, and we have used the fact that in the LIF the $\mathbf{B}$ field only has a $X^{\theta'}$ component and the magnitude is $R_{t'r'r'\phi'}X^{r'}$. Now we can see that this component is positive definite, unless the binary is aligned with the $X^{\phi'}$ axis so that $\cos[(\omega_b-\omega)\tau)]=0$. We show the value of this component in the lower panel of Fig. 5 as the blue solid curve. The red dashed line in the same panel shows the time-averaged value,

$$\langle\mathbf{e}_{r'}\cdot\mathbf{F}^B_{\rm c.m.}\rangle=\mu(\omega-\omega_b)a^2R_{t'r'r'\phi'}. \quad (23)$$

Since it is positive, we can attribute the initial upward motion of the c.m. in Fig. 4 to the $X^{r'}$ component of $\mathbf{F}^B_{\rm c.m.}$.

As soon as the c.m. leaves the origin, the centrifugal force and, more importantly, the gravitoelectric force (see the black solid curve in the lower panel of Fig. 5) start to take effect and further accelerate the c.m. As the speed increases, the Coriolis force,

$$\mathbf{F}^{\rm C}_{\rm c.m.}=-2m_{12}\boldsymbol{\omega}\times\mathbf{v}'_{\rm c.m.}, \quad (24)$$

becomes stronger and eventually exceeds the gravitoelectric force. Since the Coriolis force makes the velocity vector to rotate, the trajectory in Fig. 4 bends over and finally comes back to the $X^{\phi'}$ axis.

Interestingly, as soon as the c.m. is back on the $X^{\phi'}$ axis, its velocity in the LIF vanishes. This can be seen as a consequence of the conservation of the Jacobian energy in a rotating frame. More specifically, in our fiducial model the inner binary remains circular so that neither its internal energy nor the angular momentum significantly changes, as we have shown in the upper panel of Fig. 5. Therefore, the Jacobian energy of the outer orbit is approximately a constant. The vanishing of the velocities restores the initial condition in the LIF. As a result, the dynamical evolution described above repeats. This is the reason that the black solid curve in Fig. 4 shows a periodic pattern.

D. Evolution of the outer orbit

The difference between the outer orbit and the geodesic of a test particle can be more clearly seen in the Boyer-Lindquist coordinates, as is shown in Fig. 6. The black solid curves correspond to the results from our fiducial model. From the upper panel, we find that the c.m. periodically takes excursions to slightly larger r and comes back. The period is much longer than that of the outer orbit, as can be read from the values of the azimuthal coordinate ϕ where one orbital period corresponds to $\Delta\phi=2\pi$.

We can compare such a radial migration with the shrinkage of the outer orbit due to GW radiation. In the former case, we have seen that the radius has changed by a factor of $\Delta r/r\sim 10^{-4}$ during one to two revolutions of the outer orbit. In the latter case, where the GW radiation

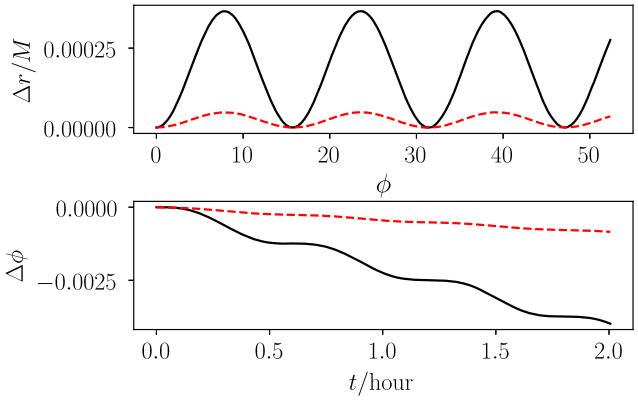

FIG. 6. Variation of the radial (upper panel) and azimuthal (lower panel) Boyer-Lindquist coordinates with respect to a circular geodesic. The black curves refer to our fiducial model in which the c.m. has no initial velocity in the FFF or LIF. The red dashed curves show the results when an initial velocity is added to the c.m. to cancel the radial component of the gravito-magnetic force (see Sec. IV A).

timescale is approximately $(M/m_{12})(r/M)^{5/2}$ times the orbital period [66], we find that the outer orbit in our fiducial model would shrink by an amount of $\Delta r/r \sim 10^{-6}$ during two orbital periods. Therefore, the GEM force could dominate the radial evolution of the outer orbit even when the system already enters the final stage of GW radiation.

The lower panel of Fig. 6 shows the difference in the orbital phase. The black solid curve suggests that the c.m. of our BBH is lagging behind the test particle on a circular orbit. The phase difference is accumulative, increasing by about 10^{-3} radian during each excursion of the c.m. As a result, we would expect a phase difference of about 0.0025 radian in one hour, or as large as 1 radian in about 17 days. Such a deviation will result in observable signatures, as we will discuss in Sec. VI.

IV. VARYING THE INITIAL CONDITIONS

A. Velocity of the c.m.

We have seen that if the outer orbit starts on a circular geodesic, it will soon deviate from circular motion by oscillating radially. The oscillation is driven initially by the gravitomagnetic force, which on average accelerates the c.m. of the BBH along the radial direction.

We notice that such a force can be balanced by the Coriolis force if we relax the initial condition, giving the c.m. of the BBH an extra velocity in the $X^{\phi'}$ (azimuthal) direction. Introducing such a Coriolis force, in principle, could reduce the radial acceleration and hence suppress the amplitude of the radial oscillation. In this way, a circular orbit may be sustained.

To test the above postulation, we give the c.m. an initial velocity along the $X^{\phi'}$ axis (z axis in the FFF). The magnitude of this velocity is given by equating Eqs. (23) and (24). To transfer this velocity into the FFF, we use the fact that initially $\mathbf{v}'_{\rm c.m.} = \mathbf{v}_{\rm c.m.}$ because $\mathbf{x}_{\rm c.m.} = 0$.

The results are shown in Fig. 6 as the red dashed curves. The upper panels shows that, indeed, the radial oscillation is significantly smaller than that in the previous case, where the c.m. has no initial velocity in the azimuthal direction. However, the amplitude of the oscillation is not zero. This can be explained by the fact that the gravitomagnetic force is oscillatory but the Coriolis force is varying more smoothly. Therefore, an initial azimuthal velocity could reduce, but not completely suppress the radial oscillation of a binary around a SMBH.

The red dashed curve in the lower panel of Fig. 6 shows that the phase shift is also much smaller when an azimuthal velocity is initially added to the c.m. of the BBH. Therefore, detecting such BBH would require much longer observing time.

B. Orientation of the inner orbit

In our fiducial model, the inner binary initially rotates in the same direction as the outer orbit. We have seen that in such a prograde case, the c.m. of the inner binary will drift in the negative azimuthal direction. If we flip the rotation axis of the inner binary to make it counterrotating with respect to the outer orbit, according to Eq. (17), then the dominant part of the gravitomagnetic force, i.e., the term proportional to $\mathbf{v}_2 - \mathbf{v}_1$, will change sign. Then the c.m. of the inner binary initially accelerates in the opposite direction relative to the fiducial case. We expect that the subsequent azimuthal drift of the c.m. will also flip direction.

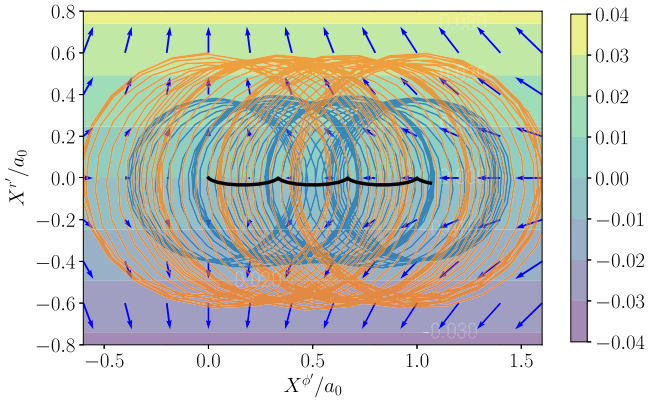

FIG. 7. Same as Fig. 4 but the BBH is rotating in the retrograde direction, i.e., the angular momentum is pointing out of the page. The c.m. of the BBH starts from the origin, $(X^{r'}, X^{\phi'}) = (0, 0)$.

Figure 7 shows the result from our simulation of a retrograde inner binary. Comparing with the trajectory of the c.m. shown in Fig. 4, we find that the inner binary indeed reverses the drift direction when its rotation axis flips. Figure 8 compares the Boyer-Lindquist coordinates of the c.m. in the prograde and retrograde cases. We can see that in both the radial (upper panel) and the azimuthal directions (lower panel), the direction of the drift flips as the sign of the angular momentum of the inner binary changes.

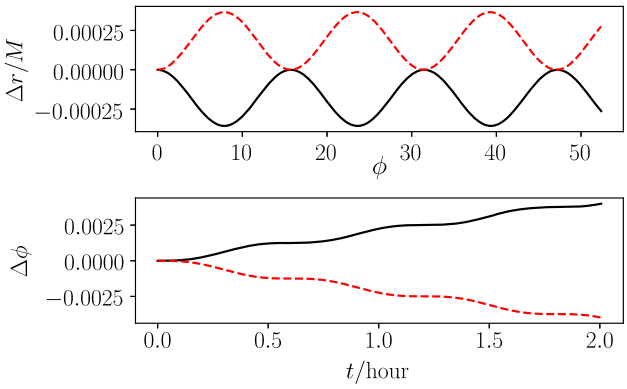

FIG. 8. Same as Fig. 6 but only showing the simulations without an initial c.m. velocity in the FFF or LIF. The black solid and red dashed curves, respectively, refer to the simulations with retrograde and prograde BBHs.

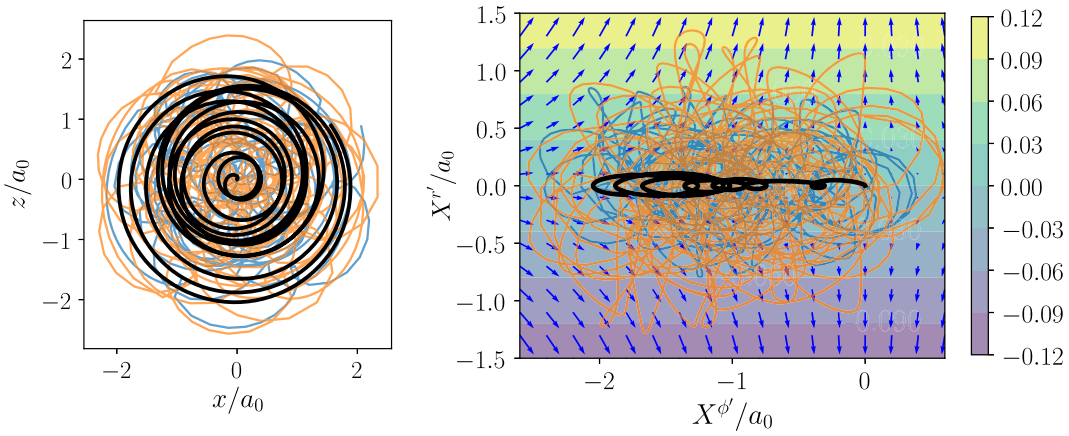

FIG. 9. Evolution of a prograde BBH when the initial distance to the SMBH is $r = 2.8M$. The left panels shows the evolution in the FFF and the right one in the LIF. The lines, arrows, and colors have the same meanings as in Figs. 3 and 4.

C. Distance to the SMBH

To study the evolution of the BBH at a smaller distance to the SMBH, we reduce the initial radius of the outer orbit to $r = 2.8M$ and rerun the simulation. The other parameters are kept the same as those in the fiducial model.

Figure 9 shows the resulting trajectories of the two stellar mass BHs and their c.m. in the FFF (left) and the LIF (right panel). We can see that the inner binary is no longer circular. The trajectory of the c.m. is also more irregular compared with that in the fiducial model. In particular, the direction of its azimuthal drift reverses several times, as can be seen in the LIF. These behaviors are qualitatively different compared with that at a larger distance from the SMBH.

To understand the cause of the irregularity, we show in the upper panel of Fig. 10 the evolution of the semimajor axis and the eccentricity of the inner binary. Now both parameters vary with significantly larger amplitude compared with the variation in the fiducial model (Fig. 5). The larger amplitude is a result of the stronger GEM forces at smaller r. Furthermore, we find that the eccentricity of the inner binary is quasiperiodically excited to a value as large as 0.9, on a timescale roughly ten times longer than the initial orbital period of the inner binary (τ_0). The evolution does not resemble the Von Zeipel–Lidov-Kozai cycle not only because of its irregularity but also because the Von Zeipel–Lidov-Kozai cycle requires the inner and outer orbits to be misaligned, but they are coplanar in our case.

The irregularity of the inner orbit also makes the GEM forces on individual BHs more complex. As is shown in the lower panel of Fig. 10, neither the gravitomagnetic nor the gravitoelectric force behaves according to a simple sinusoidal curve. However, the $X^{r'}$ component of the gravitomagnetic force remains positive, reflecting the fact that the inner binary remains rotating in the prograde direction. On the contrary, the $X^{r'}$ component of the gravitoelectric force could reach large negative values during the evolution, suggesting that the c.m. of the BBH has wandered far into the lower half-plane of the LIF.

Figure 11 shows the variation of the Boyer-Lindquist coordinates of the outer orbit. Comparing it with the results from the fiducial model, we find that the variation in the radial direction has larger amplitude now. More importantly, the amplitude seems to increase with time. This behavior

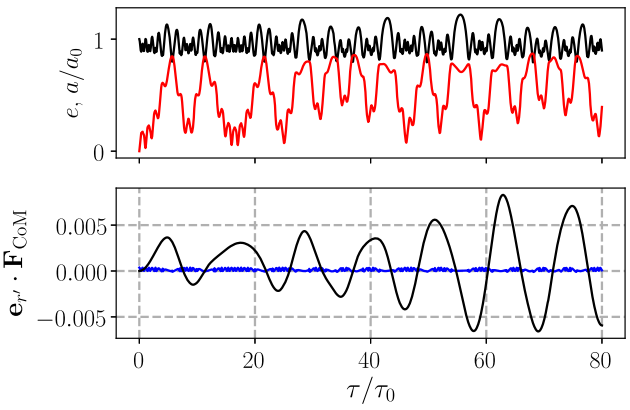

FIG. 10. The same as Fig. 5 but for $r = 2.8M$.

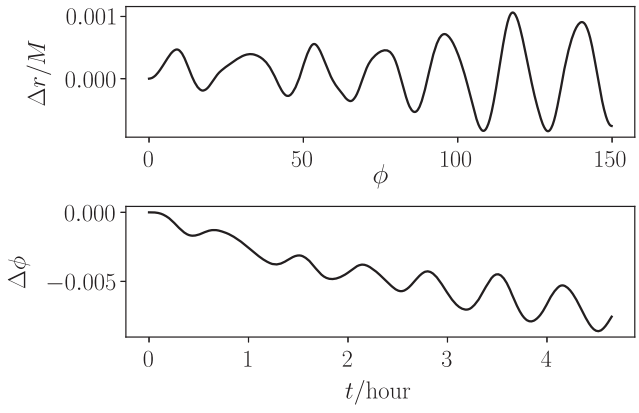

FIG. 11. The same as Fig. 6 but for $r = 2.8M$.

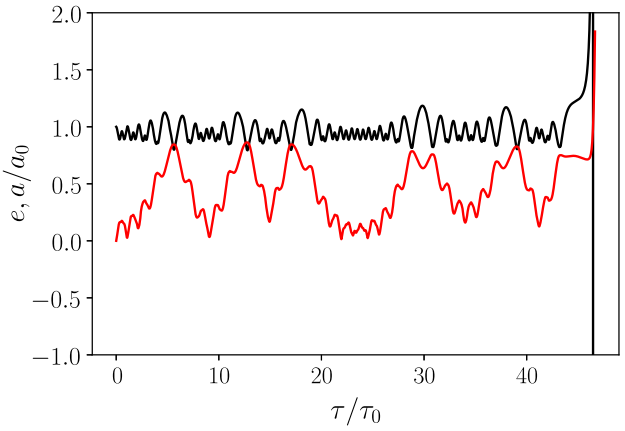

FIG. 12. The same as the upper panel of Fig. 10, but suppressing the effect of the gravitomagnetic force. Consequently, the BBH breaks by the end of the simulations.

can be understood as the consequence of an exchange of energy between the inner BBH and the outer orbit. Moreover, the phase shift in the azimuthal direction, $\Delta\phi$, also accumulates much more quickly when r is smaller. More quantitatively, the magnitude of $\Delta\phi$ could reach 0.005 radian in about two hours, which amounts to 1 radian in about eight days.

Because of its irregular variation, the gravitomagnetic force can no longer be counterbalanced by a constant Coriolis force in the LIF. Therefore, we find that introducing an initial velocity to the c.m. will not reduce the amplitude of the radial or azimuthal drift in the LIF. For this reason, we do not show the corresponding results in Fig. 11.

It is worth mentioning that the gravitomagnetic force plays an important role in stabilizing the inner binary. For example, Fig. 12 shows the evolution of the inner BBH when we suppress the gravitomagnetic force by hand. The other parameters are the same as in Fig. 10. The binary breaks after about 45 revolutions. The reason is as follows. The main effect of the gravitomagnetic force is to rotate the velocity vector of each BH. The rotation of the velocity prevents the BHs from venturing far away from the origin of the FFF. Without the gravitomagnetic force, the BHs can travel in opposite directions for a longer time. As a result, the average distance between the two BHs are larger, and the binary becomes more susceptible to tidal disruption. More importantly, since the gravitomagnetic force generally increases with the spin parameter s of the SMBH, we expect that a larger spin could in general make the BBH more stable.

V. COMPARE WITH PN SIMULATIONS

As we have mentioned at the beginning of the paper, the PN formalism is not suitable for our problem because it is derived in the limit of low velocity. To see the difference between the PN orbit and the orbit from our method, we simulate the triple evolution using the PN formalism presented in [72]. We include the terms up to 2PN order, so that the effect of spin-orbit coupling is present. We neglect the 2.5PN and higher-order terms, because they become important only after tens of thousands of revolutions of the outer orbit.

To allow easier comparison, in the PN simulation we place the c.m. of the BBH initially on a circular orbit coplanar with the equatorial plane of the spinning SMBH. Notice that the circular velocity in the PN simulation is calculated from

$$-\frac{V^2}{r_h}\mathbf{n} = -\frac{M}{r_h^2}\mathbf{n} + \frac{M}{r_h^2}\mathbf{n}(A_2 + A_4) + \mathbf{V}\times\mathbf{H}, \quad (25)$$

where $A_2 = -V^2 + 4M/r_h$ and $A_4 = -(M/r_h)^2$ [73]. The radius r_h refers to the harmonic coordinate [73]. It is related to the Boyer-Lindquist coordinate as

$$r_h = (r-M)\cos\left[\frac{s}{2\sqrt{M^2-s^2}}\ln\frac{r-r_-}{r-r_+}\right] + a\sin\left[\frac{s}{2\sqrt{M^2-s^2}}\ln\frac{r-r_-}{r-r_+}\right] \quad (26)$$

with $r_\pm = M \pm \sqrt{M^2-s^2}$, if the orbit is inside the equatorial plane [74]. The result for a test particle is

$$V_\pm = \frac{-s\alpha^2 \pm \sqrt{s^2\alpha^4 + \alpha(1-\alpha)(1-4\alpha+9\alpha^2)}}{1-\alpha}, \quad (27)$$

where $\alpha = M/r_h$ (also see [75]). We can see that it is different from the one given by Eq. (8).

We then replace the test particle with our BBH, and run three-body simulations using three different methods, namely, the 2PN formalism, our GEM method, and an additional Newtonian simulation for reference. Figure 13 compares the evolution of the inner binary when $r = 6M$. Notice that we have increased the semimajor axis of the inner binary to $a = 6000m_{12}$ to place it in the dark-shaded region in Fig. 2. The masses of the BHs and the spin of the SMBH are the same as in our fiducial model. We find that both the PN and the Newtonian simulations underestimate the variation of the semimajor axis and eccentricity of the inner binary. The difference in e is more prominent: while the variation can be as large as $\Delta e \simeq 0.6$ in our GEM simulation, the Δe given by the PN and Newtonian simulations remains smaller than 0.25. The difference also suggests that tidal force alone cannot produce the large eccentricity shown in Fig. 10.

Figure 14 shows the difference of the outer orbit given by the aforementioned three methods. We find that the Newtonian simulation gives the smallest variation in a. Both the PN and our GEM simulations result in much larger variations in a. Although the variation of a is the

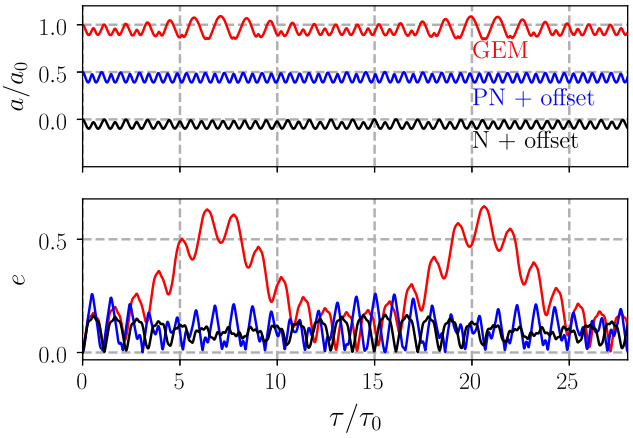

FIG. 13. Evolution of the semimajor axis (upper panel) and eccentricity (lower panel) of the inner binary based on our GEM method (red), the PN formalism (blue), and Newtonian gravity (black). Note that we have introduced a offset to the semimajor axis to show more clearly the result from each simulation. Initially, we set $r = 6M$, $a = 6000m_{12}$, and the other parameters are the same as in Fig. 10.

largest in the PN simulation, the orbital phase is different from the one given by the GEM simulation. Therefore, we conclude that the PN formalism is inadequate to simulate the system of our interest.

To test the robustness of the above conclusion, we also run simulations at $r = 10M$ with $a = 9000m_{12}$. The results are shown in Figs. 15 and 16. We can see that the difference between the GEM and PN orbits remains significant. We do not explore larger r because the GEM effect would become subdominant according to Fig. 2.

VI. OBSERVABLE SIGNATURES

In our model, we have chosen an inner binary with an orbital frequency of about 10 mHz in its rest frame. Taking into account the facts that the GW frequency of a circular binary is twice the orbital frequency and the observed frequency would be further modulated by a factor of a few due to the gravitational and Doppler redshifts [76], we find that the inner binary, i.e., the BBH, remains in the sensitive band of LISA.

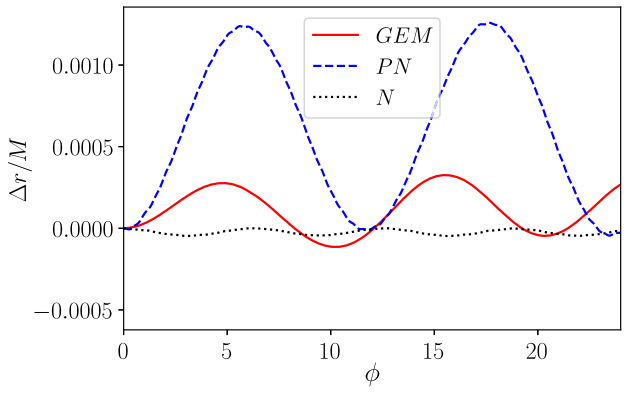

FIG. 14. Variation of the radial coordinate of the c.m. of the BBH. The red, blue, and black lines show, respectively, the results from the GEM, PN, and Newtonian simulations. The parameters are the same as in Fig. 13.

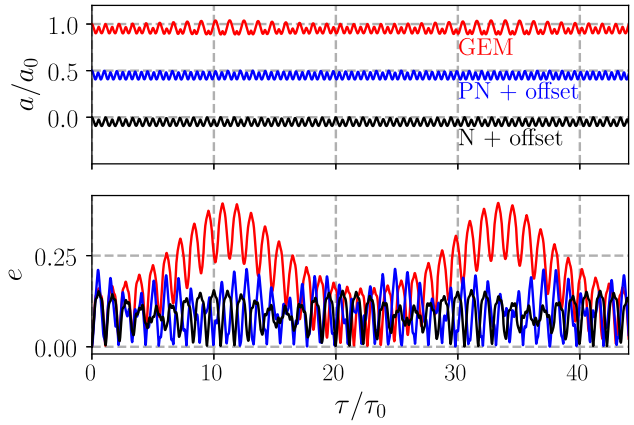

FIG. 15. The same as Fig. 13 but for $r = 10M$, $a = 9000m_{12}$.

The GW signal from such an inner binary has been studied in detail in recent years. These earlier studies have revealed a significant shift of the GW phase which can be used to distinguish the BBHs around SMBHs (see a summary in Sec. I). Here we point out an additional phase shift based on the results shown Figs. 5 and 10. We can see that the semimajor axis and eccentricity of the inner binary oscillate rapidly. The oscillation of these orbital elements will affect how the orbital phase, and hence the GW phase, increases with time. The associated timescale is the rotation period of the BBH, which is much shorter than the period of the outer orbit or the Von Zeipel–Lidov-Kozai cycle. The short timescale is closely associated with the driving mechanism, which is the variation of the GEM forces during the mutual rotation of the two small BHs. Therefore, detecting a phase shift on a timescale comparable to the period of the GWs might indicate that the BBH is close to a SMBH.

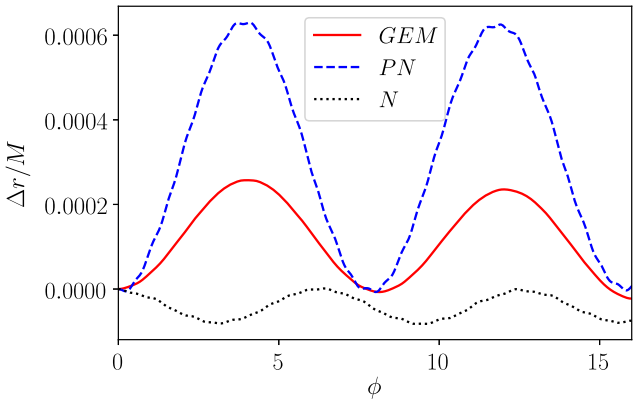

FIG. 16. The same as Fig. 14 but for $r = 10M$, $a = 9000m_{12}$.

The outer orbit of our system, seen by a distant observer, has a frequency of about 1 mHz. Therefore, the GWs emitted by the outer orbit may also be detectable by LISA. While the previous studies of similar triple systems have modeled the outer orbit with a geodetic motion (free fall), our work clearly shows that the orbit is not in free fall. In principle, the deviation is detectable by contrasting the observed signal with the template of a standard EMRI, i.e., an EMRI with only one stellar-mass BH whose mass is m_{12}. A mismatch by one radian would be sufficient to reveal the peculiarity of the small object around the SMBH. Finding such a mismatch needs only one to two weeks of data, according to the phase shifts shown in Figs. 6, 8, and 11. In practice, distinguishing such a phase shift from the effect caused by other environmental factors, such as a perturbation by the surrounding gas or stars [77–81], might be difficult and requires further investigation.

Another interesting signature revealed by our simulations is that the direction of the phase shift of the outer orbit is correlated with the orientation of the inner binary. As is shown in the lower panel of Fig. 8, a prograde inner binary drifts along the negative azimuthal direction, while a retrograde one drifts towards the positive azimuthal direction. Such a difference can be used in future EMRI observations to infer the orientations of the inner binaries. According to the previous studies, knowing the orientation would help us understand the dynamical processes responsible for the production of stellar-mass BHs around SMBHs [67–71].

VII. CONCLUSION AND FUTURE WORK

In this study, we have investigated the evolution of a BBH at a distance of only 2–3 gravitational radii from a Kerr SMBH. We showed that such a highly relativistic triple can be modeled using Newtonian dynamics plus a perturbative GEM force if one takes advantage of its hierarchy and investigate the dynamics in a frame freely falling alongside the BBH. Our main finding is that the c.m. of the BBH does not follow a geodesic line. We identified the cause of the geodetic deviation to be a nonvanishing GEM force on the c.m. We pointed out that within several weeks, the deviation will be large enough to be detectable by LISA. Find such a signal could reveal the binarity of the small object in an EMRI source, as well as put constraint on the orientation of the inner binary.

So far, we have restricted ourselves to the systems with near-circular outer orbits. Although this choice is motivated by a class of astrophysical models, our method in principle can be applied to elliptical, parabolic, or hyperbolic outer orbits with a slight modification, e.g., by choosing an appropriate free-fall observer on the same orbit. Such an improvement is useful because noncircular orbits could also be populated with BBHs due to a dynamical process called "tidal capture" [45,46].

Our current method is insufficient to track the BBH when it wanders substantially far away from the origin of the FFF. This is because when the separation between the origin of the coordinates and the c.m. of the BBH is comparable to M, the perturbation induced by the background Kerr SMBH to the metric of the FFF will no longer be small. However, as long as the size of the BBH remains small relative to M, we can circumvent the problem by resetting the FFF, making it centered on the BBH. The accuracy of such a method needs to be tested. A real difficulty is simulating an outer orbit which lies outside the equatorial plane of the central spinning SMBH. In this case, the c.m. of the BBH will oscillate up and down the equatorial plane, invalidating our method of calculating the Riemann tensor. Moreover, the Riemann tensor in the FFF becomes more asymmetric so that the c.m. of the BBH will deviate from the origin of the FFF more quickly.

We have not included the effect of GW radiation in our simulations. For the inner BBH, we can include the effect by adding PN corrections to the equation of motion since the semimajor axis a is much larger than m_{12}. These corrections will become important when the BBH obtains high eccentricity, as we have seen in the case of a small distance between the BBH and the SMBH ($r = 2.8M$). In particular, the dissipative PN terms will drive the BBH to coalesce when e is large. Therefore, we will be able to test the correlation between a small r and a higher probability of BBH coalescence, as was envisioned in [76]. For the outer orbit, the GW radiation will lead to a gradual shrinkage of r. It might result in an interesting situation in which the effect of GW radiation is counter-balanced by the increase of r as we have seen in Figs. 6 and 11. This could be a new way of trapping BBHs at the last few gravitational radii from a SMBH, in addition to the mechanism proposed in a previous work [47].

Although there is still much space for improvement, the current work has established a practical framework to quickly generate the orbit of a BBH very close to a SMBH ($r \lesssim 10M$) while keeping most of the essential relativistic effects included. This framework will also enable us to build more accurate waveform templates, which are crucial to the detection of such triple systems in future GW missions like LISA.

ACKNOWLEDGMENTS

This work is supported by the National Key Research and Development Program of China Grant No. 2021YFC2203002. X. C. is also supported by the National Science Foundation of China Grants No. 11873022 and No. 11991053. The authors would like to thank Zhoujian Cao and Bing Sun for their help in the problem of coordinate transformation.

[1] J. Weber, Phys. Rev. Lett. **25**, 180 (1970).
[2] G. A. Campbell and R. A. Matzner, J. Math. Phys. (N.Y.) **14**, 1 (1973).
[3] J. K. Lawrence, Phys. Rev. D **7**, 2275 (1973).
[4] H. C. Ohanian, Phys. Rev. D **8**, 2734 (1973).
[5] The LIGO Scientific, the Virgo, and the KAGRA Collaborations, arXiv:2111.03606.
[6] LIGO Scientific and Virgo Collaborations, Astrophys. J. Lett. **818**, L22 (2016).
[7] The LIGO Scientific and The Virgo Collaborations, Astrophys. J. Lett. **882**, L24 (2019).
[8] LIGO Scientific and Virgo Collaborations, Astrophys. J. Lett. **900**, L13 (2020).
[9] F. Antonini and H. B. Perets, Astrophys. J. **757**, 27 (2012).
[10] C. Petrovich and F. Antonini, Astrophys. J. **846**, 146 (2017).
[11] B.-M. Hoang, S. Naoz, B. Kocsis, F. A. Rasio, and F. Dosopoulou, Astrophys. J. **856**, 140 (2018).
[12] B. Liu and D. Lai, Phys. Rev. D **102**, 023020 (2020).
[13] A. Kuntz, Phys. Rev. D **105**, 024017 (2022).
[14] H. Gautham Bhaskar, G. Li, and D. N. C. Lin, Astrophys. J. **934**, 141 (2022).
[15] D. J. Muñoz, N. C. Stone, C. Petrovich, and F. A. Rasio, arXiv:2204.06002.
[16] M. C. Miller and V. M. Lauburg, Astrophys. J. **692**, 917 (2009).
[17] C. Baruteau, J. Cuadra, and D. N. C. Lin, Astrophys. J. **726**, 28 (2011).
[18] B. McKernan, K. E. S. Ford, W. Lyra, and H. B. Perets, Mon. Not. R. Astron. Soc. **425**, 460 (2012).
[19] I. Bartos, B. Kocsis, Z. Haiman, and S. Márka, Astrophys. J. **835**, 165 (2017).
[20] N. C. Stone, B. D. Metzger, and Z. Haiman, Mon. Not. R. Astron. Soc. **464**, 946 (2017).
[21] N. W. C. Leigh, A. M. Geller, B. McKernan, K. E. S. Ford, M. M. Mac Low, J. Bellovary, Z. Haiman, W. Lyra, J. Samsing, M. O'Dowd, B. Kocsis, and S. Endlich, Mon. Not. R. Astron. Soc. **474**, 5672 (2018).
[22] Y. Yang, I. Bartos, Z. Haiman, B. Kocsis, Z. Márka, N. C. Stone, and S. Márka, Astrophys. J. **876**, 122 (2019).
[23] G. Fragione, E. Grishin, N. W. C. Leigh, H. B. Perets, and R. Perna, Mon. Not. R. Astron. Soc. **488**, 47 (2019).
[24] H. Tagawa, Z. Haiman, and B. Kocsis, Astrophys. J. **898**, 25 (2020).
[25] M. Arca Sedda *et al.*, Classical Quantum Gravity **37**, 215011 (2020).
[26] M. Gröbner, W. Ishibashi, S. Tiwari, M. Haney, and P. Jetzer, Astron. Astrophys. **638**, A119 (2020).
[27] K. E. S. Ford and B. McKernan, arXiv:2109.03212.
[28] The LIGO Scientific and The Virgo Collaborations, Astrophys. J. Lett. **920**, L42 (2021).
[29] F. Zhang, X. Chen, L. Shao, and K. Inayoshi, Astrophys. J. **923**, 139 (2021).
[30] J. Samsing, I. Bartos, D. J. D'Orazio, Z. Haiman, B. Kocsis, N. W. C. Leigh, B. Liu, M. E. Pessah, and H. Tagawa, Nature (London) **603**, 237 (2022).
[31] K. Inayoshi, N. Tamanini, C. Caprini, and Z. Haiman, Phys. Rev. D **96**, 063014 (2017).
[32] Y. Meiron, B. Kocsis, and A. Loeb, Astrophys. J. **834**, 200 (2017).
[33] K. W. K. Wong, V. Baibhav, and E. Berti, Mon. Not. R. Astron. Soc. **488**, 5665 (2019).
[34] N. Tamanini, A. Klein, C. Bonvin, E. Barausse, and C. Caprini, Phys. Rev. D **101**, 063002 (2020).
[35] A. Torres-Orjuela, X. Chen, and P. Amaro-Seoane, Phys. Rev. D **101**, 083028 (2020).
[36] X. Chen and P. Amaro-Seoane, Astrophys. J. Lett. **842**, L2 (2017).
[37] A. Sesana, Phys. Rev. Lett. **116**, 231102 (2016).
[38] B.-M. Hoang, S. Naoz, B. Kocsis, W. M. Farr, and J. McIver, Astrophys. J. Lett. **875**, L31 (2019).
[39] L. Randall and Z.-Z. Xianyu, Astrophys. J. **878**, 75 (2019).
[40] P. Gupta, H. Suzuki, H. Okawa, and K.-i. Maeda, Phys. Rev. D **101**, 104053 (2020).
[41] R. S. Chandramouli and N. Yunes, Phys. Rev. D **105**, 064009 (2022).
[42] Y. Fang and Q.-G. Huang, Phys. Rev. D **99**, 103005 (2019).
[43] B. Liu, D. Lai, and Y.-H. Wang, Astrophys. J. Lett. **883**, L7 (2019).
[44] C. M. Will, Phys. Rev. D **89**, 044043 (2014).
[45] X. Chen and W.-B. Han, Commun. Phys. **1**, 53 (2018).
[46] E. Addison, M. Gracia-Linares, P. Laguna, and S. L. Larson, Gen. Relativ. Gravit. **51**, 38 (2019).
[47] P. Peng and X. Chen, Mon. Not. R. Astron. Soc. **505**, 1324 (2021).
[48] The LIGO Scientific, the Virgo, and the KAGRA Collaborations, arXiv:2111.03634.
[49] P. Amaro-Seoane, J. R. Gair, M. Freitag, M. C. Miller, I. Mandel, C. J. Cutler, and S. Babak, Classical Quantum Gravity **24**, R113 (2007).
[50] X. Chen, S. Li, and Z. Cao, Mon. Not. R. Astron. Soc. **485**, L141 (2019).
[51] A. Vijaykumar, S. J. Kapadia, and P. Ajith, Mon. Not. R. Astron. Soc. **513**, 3577 (2022).
[52] D. J. D'Orazio and A. Loeb, Phys. Rev. D **101**, 083031 (2020).
[53] H. Yu, Y. Wang, B. Seymour, and Y. Chen, Phys. Rev. D **104**, 103011 (2021).
[54] L. Gondán and B. Kocsis, Mon. Not. R. Astron. Soc. **515**, 3299 (2022).
[55] L. Sberna, S. Babak, S. Marsat, A. Caputo, G. Cusin, A. Toubiana, E. Barausse, C. Caprini, T. Dal Canton, A. Sesana, and N. Tamanini, Phys. Rev. D **106**, 064056 (2022).
[56] Y. Gong, Z. Cao, and X. Chen, Phys. Rev. D **103**, 124044 (2021).
[57] V. Cardoso, F. Duque, and G. Khanna, Phys. Rev. D **103**, L081501 (2021).
[58] A. Torres-Orjuela, X. Chen, and P. Amaro-Seoane, Phys. Rev. D **104**, 123025 (2021).
[59] W.-B. Han and X. Chen, Mon. Not. R. Astron. Soc. **485**, L29 (2019).
[60] S. Komarov, A. Gorbatsievich, and A. Tarasenko, Gen. Relativ. Gravit. **50**, 132 (2018).
[61] B. Mashhoon, arXiv:gr-qc/0311030.
[62] J. M. Bardeen, W. H. Press, and S. A. Teukolsky, Astrophys. J. **178**, 347 (1972).
[63] W. Rindler and V. Perlick, Gen. Relativ. Gravit. **22**, 1067 (1990).
[64] L. E. Kidder, C. M. Will, and A. G. Wiseman, Phys. Rev. D **47**, R4183 (1993).

[65] D. A. Nichols, R. Owen, F. Zhang, A. Zimmerman, J. Brink, Y. Chen, J. D. Kaplan, G. Lovelace, K. D. Matthews, M. A. Scheel, and K. S. Thorne, Phys. Rev. D **84**, 124014 (2011).
[66] P. Peters, Phys. Rev. **136**, B1224 (1964).
[67] Y. Yang, I. Bartos, V. Gayathri, K. E. S. Ford, Z. Haiman, S. Klimenko, B. Kocsis, S. Márka, Z. Márka, B. McKernan, and R. O'Shaughnessy, Phys. Rev. Lett. **123**, 181101 (2019).
[68] A. Secunda, J. Bellovary, M.-M. Mac Low, K. E. S. Ford, B. McKernan, N. W. C. Leigh, W. Lyra, Z. Sándor, and J. I. Adorno, Astrophys. J. **903**, 133 (2020).
[69] H. Tagawa, Z. Haiman, I. Bartos, and B. Kocsis, Astrophys. J. **899**, 26 (2020).
[70] Y.-P. Li, A. M. Dempsey, S. Li, H. Li, and J. Li, Astrophys. J. **911**, 124 (2021).
[71] J. Li, D. Lai, and L. Rodet, Astrophys. J. **934**, 154 (2022).
[72] L. E. Kidder, Phys. Rev. D **52**, 821 (1995).
[73] L. Blanchet, Living Rev. Relativity **9**, 4 (2006).
[74] Y. Zang, X. He, and Z. Cao, Classical Quantum Gravity **37**, 207002 (2020).
[75] L. Blanchet, T. Damour, B. R. Iyer, C. M. Will, and A. G. Wiseman, Phys. Rev. Lett. **74**, 3515 (1995).
[76] X. Chen, S. Li, and Z. Cao, Mon. Not. R. Astron. Soc. **485**, L141 (2019).
[77] P. Amaro-Seoane, P. Brem, J. Cuadra, and P. J. Armitage, Astrophys. J. Lett. **744**, L20 (2012).
[78] E. Barausse, V. Cardoso, and P. Pani, Phys. Rev. D **89**, 104059 (2014).
[79] A. Derdzinski, D. D'Orazio, P. Duffell, Z. Haiman, and A. MacFadyen, Mon. Not. R. Astron. Soc. **501**, 3540 (2021).
[80] L. Zwick, P. R. Capelo, E. Bortolas, V. Vázquez-Aceves, L. Mayer, and P. Amaro-Seoane, Mon. Not. R. Astron. Soc. **506**, 1007 (2021).
[81] L. Zwick, A. Derdzinski, M. Garg, P. R. Capelo, and L. Mayer, Mon. Not. R. Astron. Soc. **511**, 6143 (2022).